Research Square

Preprints are preliminary reports that have not undergone peer review.
They should not be considered conclusive, used to inform clinical practice,
or referenced by the media as validated information.

Fluoride behaviour and coupled uranium mobilisation during ammonium bifluoride treatment of uranium in-situ recovery wells: geochemical mechanisms and environmental-risk assessment

Zhanibek Seitov
Satbayev University
Yuriy Permenev
institute of high technologies
Zhiger Kenzhetayev
institute of high technologies
Abay Omarov
institute of high technologies
Bakytzhan Toktaruly
b.toktaruly@satbayev.university

Satbayev University https://orcid.org/0000-0002-4880-2606

Research Article

Keywords: Uranium, In-situ recovery, Ammonium bifluoride, Fluorite, Reactive transport, Saturation index, Decolmatation

Posted Date: June 15th, 2026

DOI: https://doi.org/10.21203/rs.3.rs-9882270/v1

License: This work is licensed under a Creative Commons Attribution 4.0 International License.
Read Full License

Fluoride behaviour and coupled uranium mobilisation during ammonium bifluoride treatment of uranium in-situ recovery wells: geochemical mechanisms and environmental-risk assessment

Zhanibek Seitov [a], Yuriy Permenev [b], Zhiger Kenzhetaev [b], Abay Omarov [b], Bakytzhan Toktaruly [a,*]

[a] *Satbayev University, 22a Satbayev Street, Almaty 050013, Kazakhstan*
[b] *Institute of High Technologies LLP, Almaty 050012, Kazakhstan*

[*] Corresponding author.
E-mail address: b.toktaruly@satbayev.university (B. Toktaruly).

Abstract

Ammonium bifluoride (NH_4HF_2) is widely used to decolmatate the process wells of uranium in-situ recovery (ISR), yet the geochemical mechanisms of fluoride fixation and the coupled mobilisation of uranium within a real productive horizon remain poorly described. Six column experiments (0–20 g/L NH_4HF_2 against 40 g/L H_2SO_4) were performed on weakly cemented sandstone from an infiltration-type uranium deposit in the Chu–Sarysu province (Kazakhstan), with independent determination of F^- (ion-selective electrode), Al, Si and U (ICP-MS), pH and Eh, and layer-resolved core analysis by XRF and ICP-MS. Four working hypotheses were tested: CaF_2-controlled fluorine fixation (H1); coupled U retention in the F-fixation zone via UO_2F_n complexes (H2); secondary colmatation at moderate doses (H3); and a non-linear Si response governed by H_2SiF_6 hydrolysis (H4). Free F^- in the effluents never exceeded 2.9 mg/L despite a charged capacity of 1250–5000 mg/L. After the optimal 12.5 g/L stage, fluorine accumulated in the core to 0.14 % with a maximum at 10–15 cm, co-located with redistributed Ca and S. Uranium was leached by 99.6 % from the inlet zone but preferentially retained at 10–15 cm (0.069 mg/g), consistent with a coupled, partial U–F immobilisation zone. Effluent Si showed a non-monotonic dose response (minimum at 5 g/L, maximum 822 mg/L at 20 g/L). The analytical limitations of ion-selective potentiometry at high Al and Fe are quantified, and a semi-quantitative fluorine mass balance is proposed. An optimal 12.5–15 g/L window maximises permeability recovery while keeping mobile fluoride below regulatory limits, providing input parameters for ISR reactive-transport models.

Keywords: Uranium; In-situ recovery; Ammonium bifluoride; Fluorite; Reactive transport; Saturation index; Decolmatation

Highlights

- Free fluoride in ISR effluent stays below 2.9 mg/L at 0–20 g/L NH_4HF_2 doses.
- Fluorine fixes in the core to 0.14 %, peaking 10–15 cm from the inlet.
- Uranium is preferentially retained in the fluoride-fixation zone of the core.
- Effluent Si is non-monotonic with dose, reflecting H_2SiF_6 formation and hydrolysis.
- An optimal 12.5–15 g/L window maximises permeability recovery safely.

1. Introduction

In-situ recovery (ISR; also termed in-situ leaching, ISL) accounts for approximately 56 % of global primary uranium production (World Nuclear Association, 2024); in the Republic of Kazakhstan, which holds about 43 % of the world market, the technology is dominant (IAEA, 2023; Mudd, 2001a). The method relies on the long-term circulation of sulfuric-acid solutions (40–50 g/L H_2SO_4) through the productive horizon, which causes secondary mineral deposits to form in the near-screen zone of the technological and production wells, progressively reducing permeability and flow rate (Mudd, 2001a; Seredkin et al., 2016). Restoring the hydrodynamic characteristics of the wells is a critical prerequisite for the environmental and economic efficiency of ISR mining (Aben et al., 2019; IAEA, 2016).

Treatment with fluoride-bearing reagents is used to decolmatate the near-screen zone; ammonium bifluoride (NH_4HF_2) is regarded as a more handling-safe alternative to liquid hydrofluoric acid, generating HF in situ in an acidic medium (Resentera et al., 2023; Shikika et al., 2021; Zhang et al., 2012). The geochemistry of HF treatments of sandstones has been studied in detail for the oil and gas industry, beginning with Smith and Hendrickson (1965), McLeod (1984) and the classic series of Fogler et al. (1975) on feldspar dissolution kinetics. Walsh et al. (1982) developed a geochemical simulator accounting for 30 aqueous species and 14 mineral phases and demonstrated that the permeability loss during HF treatment is controlled not only by dissolution but also by mandatory secondary precipitation of CaF_2, fluorosilicates (Na_2SiF_6, K_2SiF_6), $Al(OH)_3$ and AlF_3. Labrid (1975) described the thermodynamic and kinetic aspects of acidizing argillaceous sandstones; Hartman et al. (2006) quantified the dissolution kinetics of acid-sensitive aluminosilicates in HF systems; and Crundwell (2017) proposed a micro-kinetic mechanism for quartz and silica dissolution in aqueous solutions.

For ISR deposits proper, full-scale reactive-transport models have been developed: Collet et al. (2022) applied the three-dimensional HYTEC code to the large Tortkuduk deposit (Chu–Sarysu

basin, Kazakhstan); Lagneau et al. (2019) reviewed the industrial deployment of reactive-transport modelling; and Escario et al. (2023) developed a model to forecast the environmental footprint of an ISR site. In parallel, the thermodynamics of uranium in fluorine-bearing hydrothermal fluids was systematised by Xing et al. (2018) on the basis of updated thermodynamic databases (Guillaumont et al., 2003): at T < 200 °C under oxidising conditions, uranyl-fluoride complexes (UO_2F^+, UO_2F_2(aq), $UO_2F_3^-$ and $UO_2F_4^{2-}$) predominate. Catalano et al. (2006) used XAFS spectroscopy to show a systematic change in U speciation with depth in the contaminated sediments of the Hanford 300 Area; Bots et al. (2014) described the formation of stable colloidal U(VI) nanoparticles under conditions relevant to radioactive waste; and Avasarala et al. (2019) showed experimentally that bicarbonate-oxidising conditions provide efficient oxidation of U(IV) and stabilisation of U(VI) in natural deposits.

Despite the extensive theoretical and oilfield development of HF chemistry, a systematic description of fluorine behaviour and the coupled mobilisation of uranium in the system "real sulfuric-acid lixiviant – in-situ colmatant – ISR productive horizon" is absent from the literature. Most sandstone-acidizing studies have been performed on synthetic colmatants or model quartz-sand samples (Fogler et al., 1975; Crundwell, 2017; Kenzhetayev et al., 2024) at HF concentrations of 1–6 % and under redox conditions that do not match the ISR scenario (low pH, high Eh, high contents of U, S, Al and Fe). Current ISR modelling studies (Collet et al., 2022; Lagneau et al., 2019; Escario et al., 2023) operate with averaged mineralogical parageneses and do not spatially resolve fluoride behaviour at the scale of the near-screen zone (metres from the borehole), equivalent to a long column at the laboratory scale. The analytical aspects — above all the underestimation of total soluble fluorine by ion-selective potentiometry with TISAB-II buffer at Al and Fe concentrations above 500 mg/L (Kataoka et al., 2009; Patel et al., 2018) — are traditionally underrated and lead to systematic errors in mass-balance calculations.

In the present work, column experiments on real core material from the productive horizon of an infiltration-type uranium deposit in the Chu–Sarysu province were used to test four working hypotheses concerning the mechanisms of fluorine fixation and coupled uranium mobilisation during NH_4HF_2 treatment (Section 2). The objectives were: (i) to quantitatively characterise the migration of F^- and associated components (Al, Si, Fe, Ca, U) at NH_4HF_2 doses of 0–20 g/L; (ii) to test the proposed geochemical mechanisms of solid-phase fluoride fixation and secondary U accumulation; (iii) to compare the data with the thermodynamic and kinetic database (Fogler et

al., 1975; Walsh et al., 1982; Xing et al., 2018) and with current ISR reactive-transport models (Collet et al., 2022; Lagneau et al., 2019; Escario et al., 2023); and (iv) to formulate the concentration thresholds at which decolmatation efficiency is achieved with a minimum concentration of mobile F species in the productive solution.

2. Theory and working hypotheses

2.1. Fluorine speciation in an acidic sulfate medium

The behaviour of fluorine in the system H_2SO_4 – NH_4HF_2 – Ca^{2+} – Al^{3+} – Fe^{3+} – $Si(OH)_4$ is governed by three classes of equilibria: acid–base ($HF \rightleftharpoons H^+ + F^-$; $pK_a = 3.17$ at 25 °C), complex-forming (Al, Fe and UO_2 with F^-), and mineral-forming (CaF_2, AlF_3, MgF_2, fluorosilicate precipitation). At pH < 3.2, more than 50 % of the fluoride exists as neutral HF(aq), ensuring kinetically rapid dissolution of aluminosilicate colmatants (Fogler et al., 1975; Crundwell, 2017). The trivalent cations Al^{3+} and Fe^{3+} at concentrations typical of ISR sulfuric-acid lixiviants (Al 1000–3700 mg/L, Fe 50–500 mg/L) form stable complexes AlF^{2+}, AlF_2^+, AlF_3(aq), FeF^{2+}, FeF_2^+, with stability-constant logarithms $\log\beta_1$ = 6.1–6.2 (Al) and 5.2 (Fe), effectively binding a significant fraction of dissolved fluorine into forms not detected by the ion-selective electrode with TISAB-II buffer (Kataoka et al., 2009; Patel et al., 2018).

The saturation index (SI) of fluorite is calculated as $SI(CaF_2) = \log(IAP/K_{sp})$, where IAP is the ion activity product and $K_{sp}(CaF_2) = 3.45 \times 10^{-11}$ ($\log K_{sp} \approx -10.46$; within the literature range −10.46 to −10.57, Parkhurst and Appelo, 2013; Zhang et al., 2023). Precipitation becomes thermodynamically allowed at SI > 0; under strong kinetic inhibition of fluorite formation in mixed silicate systems (Walsh et al., 1982; Zhang et al., 2023), actual precipitation may be delayed to SI ≥ 1.0–1.5 (a “supersaturation window”). Similarly, for gypsum, $SI(CaSO_4 \cdot 2H_2O)$ is determined from $[Ca^{2+}] \cdot [SO_4^{2-}]/K_{sp}$(gypsum) ($K_{sp} \approx 2.4 \times 10^{-5}$); at typical $[Ca^{2+}]$ = 0.5–2.0 g/L and $[SO_4^{2-}]$ = 20–40 g/L in ISR lixiviants, the system is always supersaturated with respect to gypsum, whose precipitation is governed by kinetics and the spatial distribution of activities along the filtration flow (Parkhurst and Appelo, 2013).

2.2. Silica solubility and fluorosilicate behaviour

Silicon in the HF – H_2O system reacts via a two-stage scheme: hexafluorosilicic acid forms first ($SiO_2 + 6HF \rightleftharpoons H_2SiF_6 + 2H_2O$), then H_2SiF_6 hydrolyses with reverse precipitation of

amorphous silica as HF is depleted ($H_2SiF_6 + 2H_2O \rightleftharpoons SiO_2(am) + 6HF$) (Fogler et al., 1975; Walsh et al., 1982; Crundwell, 2017). This leads to a non-linear dependence of effluent Si on fluoride-reagent dose: at low NH_4HF_2 concentrations, a significant fraction of Si is converted into SiF_6^{2-} complexes (not detected by ICP-MS without special preparation), whereas at high concentrations the balance shifts towards fully soluble forms with simultaneous intense matrix dissolution. Walsh et al. (1982) showed that, above a critical HF concentration specific to each mineral assemblage, precipitation of K_2SiF_6, Na_2SiF_6, $Al(OH)_3$ and amorphous SiO_2 forms secondary colmatation deposits.

2.3. Uranium speciation in a fluorine-bearing sulfate medium

Under oxidising conditions (Eh > +400 mV) and pH < 2, uranium occurs as the uranyl ion UO_2^{2+}, forming stable complexes with sulfate and fluoride: $UO_2SO_4(aq)$ ($\log\beta_1 = 2.96$), $UO_2(SO_4)_2^{2-}$ ($\log\beta_2 = 4.01$), UO_2F^+ ($\log\beta_1 = 5.16$), $UO_2F_2(aq)$ ($\log\beta_2 = 8.83$), $UO_2F_3^-$ ($\log\beta_3 = 10.9$), $UO_2F_4^{2-}$ ($\log\beta_4 = 11.84$); all constants follow NEA-TDB recommendations (Guillaumont et al., 2003; Langmuir, 1978) and the compilation of Xing et al. (2018). In the background sulfate medium of a typical ISR lixiviant, sulfate complexes predominate; on introduction of NH_4HF_2, the proportion of uranyl-fluoride forms increases substantially with each order-of-magnitude rise in $[F^-]$. The thermodynamic calculations of Xing et al. (2018) were performed for hydrothermal fluids (T = 25–450 °C, P up to 600 bar, NaCl background), whereas the present laboratory system corresponds to atmospheric conditions (T = 20–22 °C, P = 1 atm, H_2SO_4 40 g/L sulfate background); a direct transfer of their conclusions is therefore incorrect. Nevertheless, the low-temperature trend of UO_2F_n-form predominance with increasing $[F^-]$ is supported by independent NEA-TDB constants (Guillaumont et al., 2003) and by Langmuir (1978) for sedimentary conditions, whereas in the ISR sulfate medium the $UO_2SO_4(aq)$ and $UO_2(SO_4)_2^{2-}$ complexes compete with the fluoride forms. With this caveat, a testable hypothesis (rather than a proven mechanism) is formulated: the zone of elevated $[F^-]$ acts not only as a region of dissolution but also as a potential local uranium trap through mobilisation → transport as UO_2F_n → supersaturation and co-precipitation as $[F^-]$ falls along the filtration path.

Additional mechanisms for secondary U immobilisation in the F-fixation zone include: (i) sorption of UO_2^{2+} onto freshly formed Fe(III) hydroxides generated upon neutralisation of HF by reaction with Fe minerals (Catalano et al., 2006); (ii) co-precipitation of UO_2^{2+} with gypsum, by

analogy with U sorption onto calcites (Catalano et al., 2006; Avasarala et al., 2019); and (iii) the formation of colloidal U(VI) nanoparticles (Bots et al., 2014). By analogy with the phosphate barrier technology of Shi et al. (2009) and the apatite barrier technology of Vermeul et al. (2009), these mechanisms may underpin the interpretation of the observed U localisation.

2.4. Working hypotheses

On the basis of the framework above, four working hypotheses are tested.

H1 (F fixation through CaF_2 precipitation). During filtration of NH_4HF_2 through the carbonate–silicate sandstone, spatially separated zones are expected. In the strongly acidic medium (pH 0.6–1.0, H_2SO_4 40 g/L), the primary process is sulfuric-acid dissolution of carbonate with release of Ca^{2+} (Eq. 1a); the liberated Ca^{2+} is then competitively bound by fluoride into fluorite (Eq. 1b) and by sulfate into gypsum (Eq. 1c), the pathway being set by the local SI(CaF_2) and SI($CaSO_4 \cdot 2H_2O$). *Prediction:* the F maximum in the core coincides with the zone where SI(CaF_2) first becomes positive, with S accumulation as a gypsum marker somewhat deeper.

$$CaCO_3 + H_2SO_4 \rightarrow Ca^{2+} + SO_4^{2-} + H_2O + CO_2(g) \quad (1a)$$

$$Ca^{2+} + 2F^- \rightarrow CaF_2(s) \quad (1b)$$

$$Ca^{2+} + SO_4^{2-} + 2H_2O \rightarrow CaSO_4 \cdot 2H_2O(s) \quad (1c)$$

H2 (coupled U accumulation in the F-fixation zone). Uranium mobilised in the upper zone as UO_2^{2+}/UO_2SO_4 transforms into $UO_2F_n^{2-n}$ in the [F^-] maximum and, upon the subsequent [F^-] decrease, undergoes reverse desorption/precipitation. *Prediction:* the core U content shows a maximum coinciding in depth with the F maximum, exceeding adjacent segments many-fold.

$$UO_2^{2+} + nF^- \rightleftharpoons UO_2F_n^{(2-n)}; \quad n = 1–4 \quad (2)$$

H3 (non-monotonic permeability with a minimum at moderate doses). At an NH_4HF_2 concentration insufficient to fully mobilise dissolution products but sufficient to destabilise the kaolinite–hydromica fraction, secondary colmatation is expected through colloidal mobilisation of fines and/or precipitation of fluorosilicates. *Prediction:* a local minimum, deviating from the trend of the other regimes, appears on the dose curve of cumulative effluent recovery.

$$K^+ + 2F^- + SiF_4(aq) \rightarrow K_2SiF_6(s) \quad (3)$$

H4 (non-monotonic effluent Si through H_2SiF_6 hydrolysis). Effluent Si shows a minimum at low NH_4HF_2 doses owing to conversion of Si into SiF_6^{2-} forms, followed by an increase at higher doses as fully soluble forms prevail. *Prediction:* a paradoxical decrease in [Si] at the minimum fluoride dose (5 g/L) relative to the fluoride-free control, followed by a monotonic increase.

$$SiO_2(am) + 6HF \rightleftharpoons H_2SiF_6 + 2H_2O \quad (4)$$

3. Materials and methods

3.1. Study object and core material

Core material was sampled from the productive ore-bearing horizon of an infiltration-type uranium deposit mined by ISR within the Chu–Sarysu uranium-ore province (Republic of Kazakhstan). Lithologically, the rock is a weakly cemented fine-grained sandstone with siltstone and mudstone interbeds, a bed thickness of 5.2 m and an effective porosity of 30–35 %. The principal rock-forming components are quartz, plagioclase and potassium feldspars; the clay fraction comprises kaolinite and hydromica minerals with subordinate montmorillonite; the carbonate cement is calcite and dolomite; and the disseminated sulfide phase is pyrite. The averaged elemental composition of the initial core by XRF is: Si 26.25 %, Al 7.84 %, Fe 3.28 %, K 0.96 %, Ca 0.65 %, Mg 0.89 %, Ti 1.08 %, S 0.20 %; F below the method detection limit. The U content of the initial core by ICP-MS after acid digestion is 0.165 mg/g, corresponding to industrial values for the roll-front uranium deposits of the Chu–Sarysu basin (Taran et al., 2023; Collet et al., 2022).

3.2. Column experiment design



Fig. 1. Column setup (internal diameter 50 mm, core-pack height 20 cm) during filtration of the sulfuric-acid–fluoride solution, showing zones of colour change along the height that reflect the reaction front and the spatial redistribution of interaction products.

The column setup consists of a vertical transparent tube (internal diameter 50 mm, total height 1 m) with an inlet port in the upper cap and a filtering partition with an outlet port at the bottom. For each stage, a fresh charge of air-dry core weighing 500.0 ± 1.0 g (pack height 20 cm) was used, poured in while preserving its natural loose packing. Solutions were delivered by gravity from top to bottom under a liquid-column height of ≈80 cm. Six independent regimes were run, differing only in the ammonium-bifluoride concentration in the decolmatation step (0.4 L of NH_4HF_2 solution at 0, 5, 8, 20, 15 and 12.5 g/L against a 40 g/L H_2SO_4 background), followed by a wash with 1.2 L of fluoride-free 40 g/L H_2SO_4. The liquid-to-solid ratio was 3.2; the separation into a “fluoride” (0.4 L) and a “wash” (1.2 L) step reproduces the industrial ISR well-treatment scheme at a decolmatation-solution volume of about 4 m^3 per 1 m radius of the near-screen zone. The temperature was 20–22 °C. Each stage was performed on a separate charge to exclude a “sample memory” effect; the time of appearance of the first effluent drop, the interval flow rates and the fractional samples were recorded.

3.3. Analytical methods

Fractional samples were collected sequentially over the filtration cycle; for free F^-, the representative fractions reported below were taken at hours 1, 3, 5 and 7 (Table 1; Fig. 3), whereas the total effluent volume was recorded at the end of the 9-hour cycle (Fig. 2). The free fluoride-ion concentration was determined using a fluoride-selective electrode with a CDTA-based TISAB-II total-ionic-strength adjustment buffer on an ionometer with a two-point calibration in the range 0.1–100 mg/L NaF (limit of quantification 0.1 mg/L F^-). TISAB-II masks Al only partially and, at Al > 500 mg/L, gives a systematic underestimation of total soluble fluorine (Kataoka et al., 2009; Patel et al., 2018); this aspect is discussed in Section 5.5. The Al, U and Si concentrations were determined by inductively coupled plasma mass spectrometry (ICP-MS) with an octopole reaction cell using accredited in-house procedures and certified standards (relative error ≤10 %). In parallel, pH (combined glass electrode) and the redox potential (Eh, versus Ag/AgCl, converted to the standard hydrogen electrode, SHE) were recorded for each sample.

Layer-resolved core analysis was performed after removal from the column and cutting into four height segments: 0–5 cm (top, at the inlet), 5–10 cm, 10–15 cm and 15–20 cm (bottom, at the outlet). X-ray fluorescence (XRF) was performed on an Axios 1 kW wavelength-dispersive spectrometer (PANalytical) in pressed-powder mode; spectra were processed in SuperQ using the standardless Omnian 37 program (relative error ±20 %). Mass-spectrometric analysis of the core was performed after acid digestion (HNO_3 + HF + HCl) by ICP-MS (relative error ≤10 %). Identification of secondary mineral phases by X-ray diffraction (XRD) and scanning electron microscopy with energy-dispersive spectrometry (SEM-EDS) was not performed here and will be the subject of further research (Section 5.8).

3.4. Selection of Stage 5 as the reference stage

In the preliminary hydrodynamic test, Stage 5 (NH_4HF_2 12.5 g/L) gave the largest cumulative effluent recovery (1380 mL, 86 %) and the shortest time to the first drop (≈1.5 h). For a single replicate (n = 1), the difference between Stage 5 (1380 mL) and Stage 4 (15 g/L; 1200 mL) is 13 % and may lie partly within the reproducibility associated with differences in the packing of independent charges; the selection of Stage 5 as the reference is therefore pragmatic (it also corresponds to the recommended working concentration; Section 5) and does not imply statistically proven superiority over Stage 4, which gave the maximum U recovery (up to 68 mg/L) and could serve as an alternative reference. Accordingly, the spatially resolved XRF and ICP-MS

data are presented predominantly for the Stage 5 samples, with data from the other stages used for the context of the effluent dose-dependence.

3.5. Mass-balance and interpretation approach

For each stage the following were calculated: (i) the integral F^- export with the effluent as the sum of the products of F^- concentrations and fraction volumes; (ii) the mass of fluorine fixed in the core from the XRF data and charge mass; and (iii) the balance deficit as the difference between the introduced F mass (corrected for NH_4HF_2 stoichiometry) and the sum of effluent export and core fixation. The deficit is interpreted as the sum of analytically invisible forms: fluoride-complex soluble species (AlF_n, FeF_n, SiF_6^{2-}) not detected by the ISE; the colloidal–gel fraction not exported; and the systematic XRF error (±20 %). For U, the total core content ($\int c(z)\,dz$ over the segments) and its ratio to the integral effluent export were calculated. Quantitative closure through thermodynamic modelling in PHREEQC v3 (Parkhurst and Appelo, 2013) with the llnl.dat and sit.dat databases is planned for a subsequent publication.

4. Results

4.1. Hydrodynamic response to reagent dose

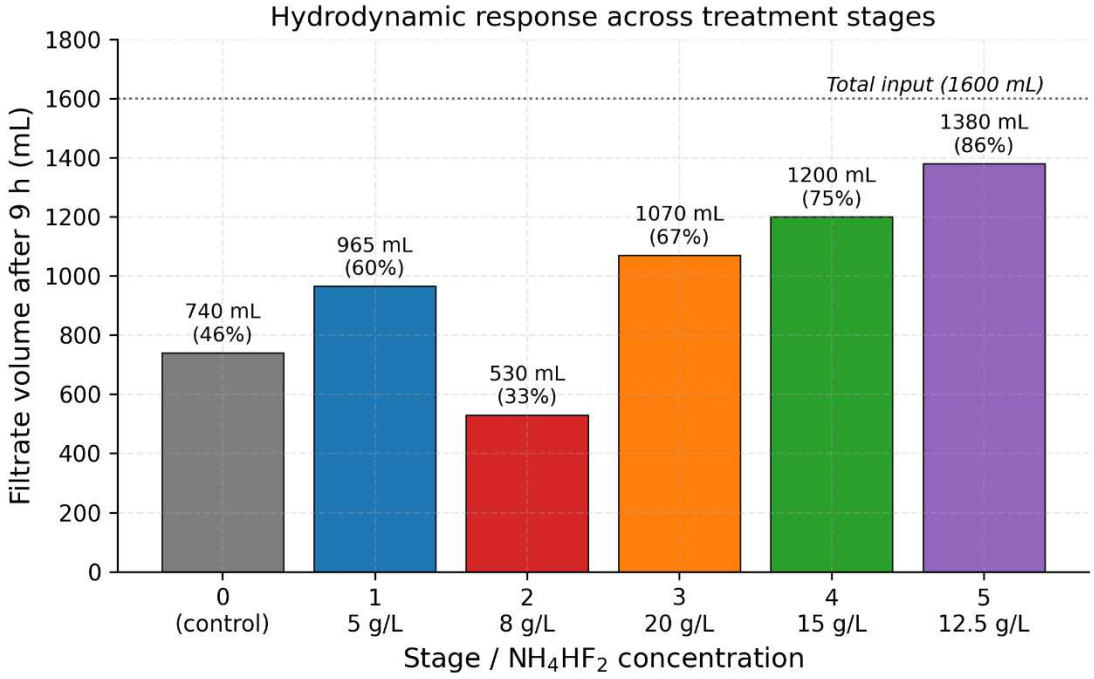


Fig. 2. Cumulative effluent volume over the 9-hour cycle, ordered by increasing NH_4HF_2 dose (each stage is an independent core charge, n = 1). The control (0 g/L) yields 740 mL (46 %); the

maximum, 1380 mL (86 %), occurs at 12.5 g/L; a local minimum of 530 mL (33 %) at 8 g/L falls below the control level (dashed line). Effluent volume is used as an indirect proxy for permeability.

The cumulative effluent volume over the fixed cycle was used as an indirect proxy for permeability recovery; direct measurement of the hydraulic conductivity K (mD) before and after treatment was not performed here and is deferred to further research (Section 5.8). The dependence of cumulative effluent recovery on NH_4HF_2 dose (Fig. 2) shows a non-linear dose optimum: the cumulative volume increases from 740 mL (Stage 0) to 1380 mL (Stage 5; 12.5 g/L) but, at 8 g/L (Stage 2), falls to 530 mL, below the control acid treatment. A further increase to 20 g/L brings no proportional gain (1070 mL). This non-monotonicity is consistent with the prediction of hypothesis H3 (secondary colmatation at intermediate concentrations through colloidal mobilisation and/or fluorosilicate precipitation); the conclusion is based on a single series per stage (n = 1), so the wording "consistent with H3", rather than "confirms", reflects the status of the observation (Section 5.3).

4.2. Free fluoride-ion concentration in the effluents

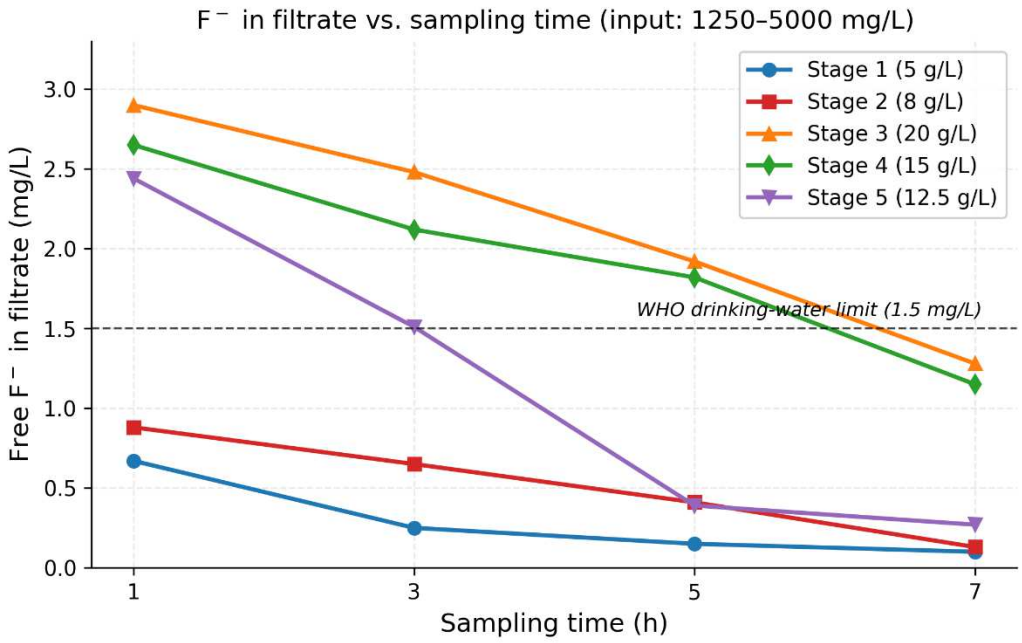


Fig. 3. Free fluoride-ion concentration in the effluent versus sampling time at different NH_4HF_2 doses (charged fluoride capacity in parentheses: 1250–5000 mg/L). Concentrations do not exceed 2.9 mg/L in the first sample and decrease to 0.1–1.3 mg/L by 7 h in all regimes. The horizontal dashed line is the WHO drinking-water guideline (1.5 mg/L; WHO, 2017).

Free F^- in all effluent fractions and regimes was 2–4 orders of magnitude below the charged capacity (Table 1; Fig. 3). The maximum values of 2.9 and 2.65 mg/L were recorded in the first samples of Stage 3 (20 g/L) and Stage 4 (15 g/L). By the 7th hour, concentrations decreased to 0.1–1.3 mg/L. The integral F export for Stage 5 (12.5 g/L) was < 1 mg F^- against an introduced mass of 1250 mg F, i.e. less than 0.1 % of the reagent in the mobile form detected by the ISE. This does not in itself close the fluorine balance, since the ISE does not account for fluoride-complex forms (Section 5.6).

Stage	NH_4HF_2 (g/L)	F^- in (mg/L)	1 h	3 h	5 h	7 h
1	5	1250	0.67	0.25	0.15	0.10
2	8	2000	0.88	0.65	0.41	0.13
3	20	5000	2.90	2.48	1.92	1.28
4	15	3750	2.65	2.12	1.82	1.15
5	12.5	3125	2.44	1.51	0.39	0.27

Table 1. Free fluoride-ion content in the effluents (mg/L) by sampling time (ISE with TISAB-II).

4.3. Dose-dependence of Al, Si, U and pH/Eh

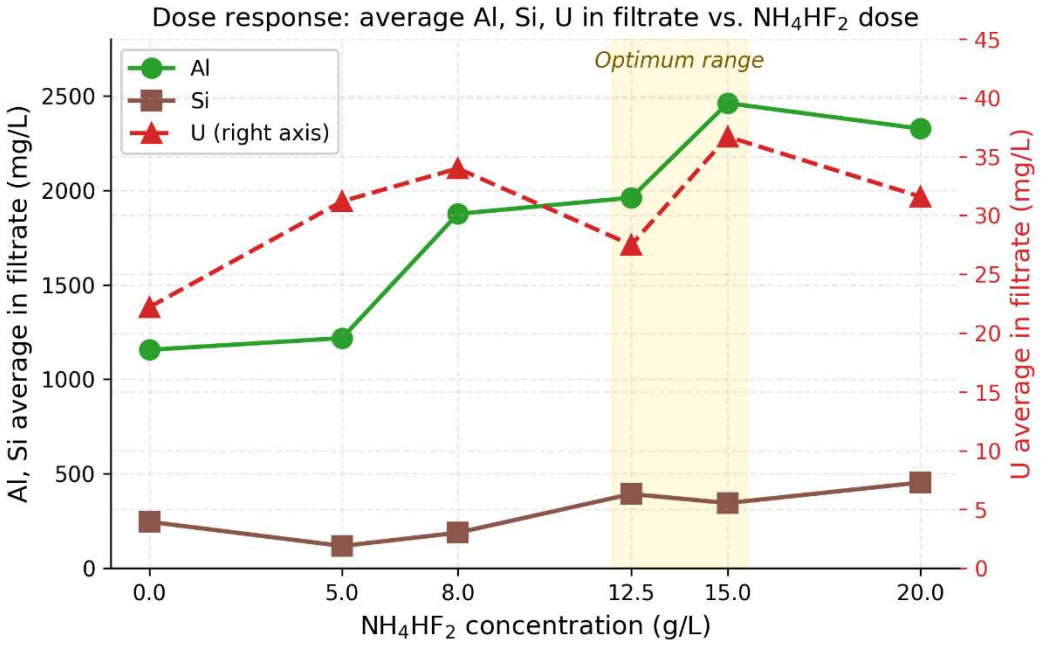


Fig. 4. Mean Al, Si and U concentrations in the effluent versus NH_4HF_2 dose (ordered by increasing dose). Al and Si show a pronounced non-linear response, with a local Si minimum at 5 g/L (hypothesis H4) and an Al maximum at 15 g/L. The shaded band at 12.5–15 g/L marks the optimal range: maximum permeability recovery (Fig. 2) while keeping free F^- below regulatory

levels (Fig. 3). The elevated U at 15 g/L (up to 68 mg/L) is not an environmental drawback: in ISR, dissolved uranium is the target product recovered at the sorption stage.

Aluminium concentrations lie in the range 1004–3683 mg/L (Table 2; Fig. 4) and show a distinct dependence on dose: ordered by increasing dose, the mean values are 1156 (0 g/L), 1218 (5 g/L), 1875 (8 g/L), 1961 (12.5 g/L), 2461 (15 g/L) and 2326 mg/L (20 g/L), rising to a maximum at 15 g/L and then plateauing. Silicon shows an even more pronounced response: at Stage 1 (5 g/L) the mean is 118 mg/L — below the control 246 mg/L (Stage 0) — thereafter increasing monotonically to 188, 393, 454 and 345 mg/L at Stages 2, 5, 3 and 4; the Si maximum (822 mg/L) was recorded in sample 2 of Stage 3. Uranium varies from 12 to 68 mg/L and reflects, above all, the overall degree of decolmatation rather than the reagent itself, with the maximum (68 mg/L) at Stage 4. The effluent pH reflects the acid-consuming capacity of the rock (first samples pH 1.1–2.5, stabilising at 0.6–1.0), while Eh lies in +445 to +479 mV versus SHE, corresponding to active oxidative leaching of U(VI) and stability of Al(III) and Fe(III) fluoride complexes (Xing et al., 2018; Catalano et al., 2006).

Stage	NH_4HF_2 (g/L)	Al (mg/L)	Si (mg/L)	U (mg/L)	pH	Eh (mV)
0	—	1004–1375	207–296	13.4–34.8	0.7–2.5	446–468
1	5	1021–1363	87–141	20.5–47.3	0.4–1.8	453–466
2	8	1650–2055	161–203	28.8–48.7	0.8–1.3	459–479
3	20	1850–2620	253–822	18.7–52.6	0.9–1.7	450–462
4	15	1680–3683	186–648	16.5–68.3	0.8–1.7	445–460
5	12.5	1557–2507	214–648	12.1–47.9	0.8–1.1	454–463

Table 2. Summary characteristics of the effluents by stage (ICP-MS for Al, Si, U; potentiometry for pH/Eh; n = 5–6 samples per stage).

4.4. Vertical distribution of F, Ca, S in the core (Stage 5)

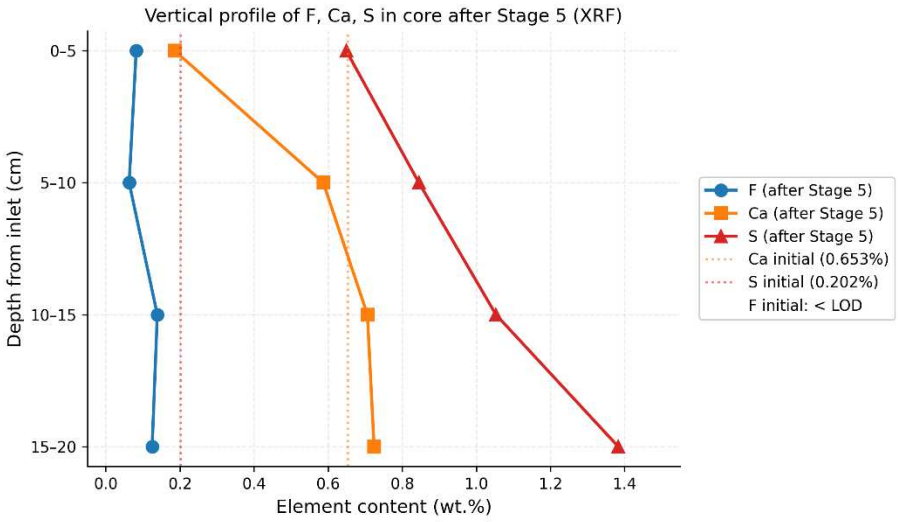


Fig. 5. Vertical profile of F, Ca and S in the core after Stage 5 (XRF). Fluorine is present in all segments (0.063–0.139 %) with a maximum at 10–15 cm. Calcium is reliably leached from 0–5 cm (loss of 71.5 % relative to the initial 0.653 %); the apparent +10.9 % gain at 15–20 cm lies within error. Sulfur increases reliably towards the bottom (0.649 → 1.383 % against the initial 0.202 %). F is plotted on a separate upper axis; error bars are ±20 % (rel.).

Layer-resolved XRF after Stage 5 (Table 3; Fig. 5) shows pronounced vertical redistribution. Fluorine, initially below detection, reaches 0.063–0.139 % with a maximum at 10–15 cm. Calcium is depleted in the upper segment (0.186 %; loss of 71.5 % relative to 0.653 %) and accumulated in the lower segment (0.724 %; +10.9 %). Sulfur increases progressively down the column (0.649 → 1.383 %), characteristic of gypsum precipitation as the H^+ activity falls. The coincidence of the F maximum with the zones of Ca and S accumulation matches the prediction of hypothesis H1 and is interpreted as mixed CaF_2–$CaSO_4 \cdot 2H_2O$ mineralisation in the middle–lower segment.

Segment	F (%)	Ca (%)	Al (%)	Fe (%)	S (%)	Si (%)
Initial core	< LOD	0.653	7.836	3.278	0.202	26.251
0–5 cm	0.082	0.186	6.681	2.348	0.649	27.676
5–10 cm	0.063	0.587	6.909	2.735	0.845	26.537
10–15 cm	0.139	0.706	7.812	2.941	1.053	27.179
15–20 cm	0.125	0.724	7.617	3.126	1.383	26.568

Table 3. Vertical distribution of the main elements in the core after Stage 5 (XRF, Axios 1 kW; relative error ±20 %). LOD, limit of detection.

4.5. Vertical distribution of Al, Fe, Si in the core (Stage 5)

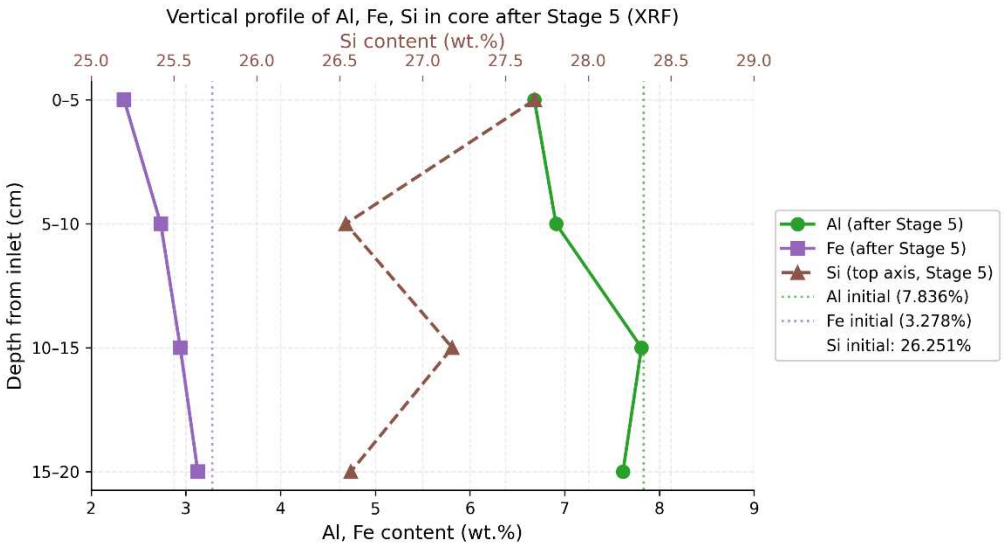


Fig. 6. Vertical profile of Al, Fe and Si in the core after Stage 5 (XRF). Al and Fe are reliably depleted only in the upper 0–5 cm segment (−1.16 and −0.93 pp); elsewhere they are statistically indistinguishable from the initial values within ±20 % (rel.). The apparent V-shaped Si profile lies entirely within the ±5.2 pp error and is not significant.

Aluminium and iron show consistent upper-segment depletion (Al 6.681 %, Fe 2.348 % against the initial 7.836 and 3.278 %; losses of 1.16 and 0.93 pp) and a return towards initial values in the middle–lower segments (Fig. 6). In no segment do Al and Fe exceed the initial values: in the lower segments they are statistically indistinguishable from the initial values within ±20 %, whereas in the upper segment the depletion is directional and significant, consistent with dissolution of the hydromica–kaolinite fraction in the upper zone and transfer of Al/Fe in mobile complex forms. The Si content in all segments (26.5–27.7 %) is comparable to the initial value (26.251 %) within the analytical error: for the standardless semi-quantitative Omnian 37 analysis, ±20 % (rel.) corresponds to ±5.2 pp for Si at the ≈26 % level, far exceeding the observed deviations (up to 1.4 pp). The weak kinetic susceptibility of quartz to fluoride treatment in this dose range is consistent with the micro-kinetic analyses of Crundwell (2017) and Fogler et al. (1975).

4.6. Uranium redistribution in the core (Stage 5)

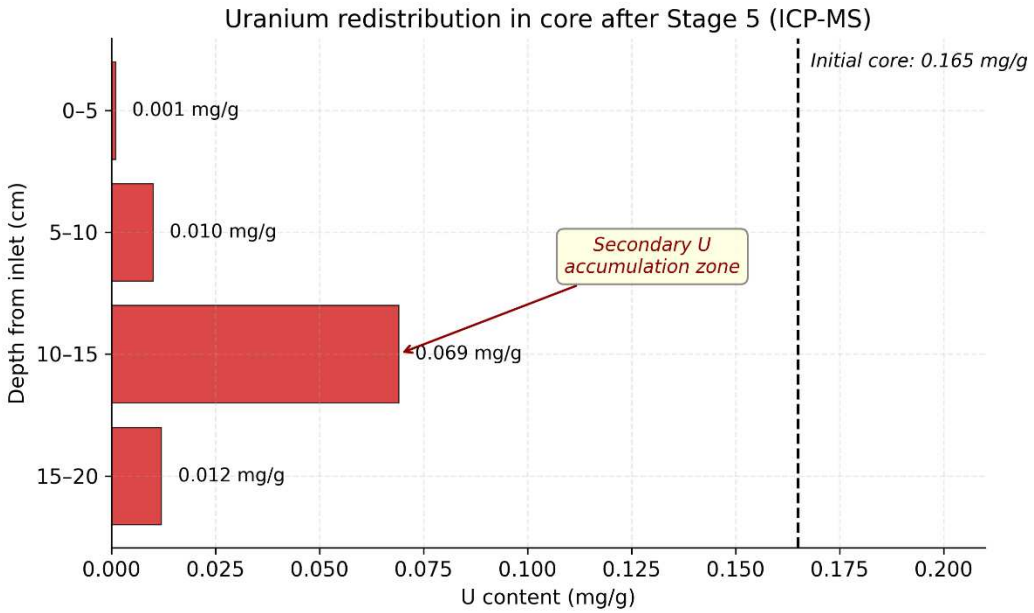


Fig. 7. Uranium distribution in the core after Stage 5 (ICP-MS). Uranium is leached by 99.6 % from 0–5 cm (0.001 vs 0.165 mg/g in the initial core); at 10–15 cm it is leached least (0.069 mg/g), 6.9 times higher than the adjacent 5–10 cm segment but still 2.4 times below the initial level. The U-retention zone coincides in depth with the F-fixation maximum (hypothesis H2). Error bars are ±10 % (rel.); the 5–10 and 15–20 cm segments are statistically indistinguishable.

The U content after Stage 5 is 0.001 mg/g at 0–5 cm (loss of 99.6 % relative to 0.165 mg/g), 0.010 mg/g at 5–10 cm, 0.069 mg/g at 10–15 cm, and 0.012 mg/g at 15–20 cm. The ratio between the 10–15 cm and 0–5 cm segments is 69-fold; for the segments adjacent to the retention zone the ratios are 6.9 (10–15 vs 5–10 cm) and 5.8 (10–15 vs 15–20 cm). The integral U balance (equal segment mass of 125 g) gives a total after Stage 5 of ≈11.5 mg against the initial 82.5 mg in the 500 g charge, i.e. about 14 % of the initial U is retained, of which ≈75 % is in the 10–15 cm segment. The U retention coincides in depth with the F maximum (0.139 %), whereas the Ca maximum (0.724 %) is one segment lower (Section 5.1). Analogous accumulation was recorded for Pb (maximum 0.011 mg/g in the lower segment) and Mn (0.025–0.028 mg/g versus 0.013–0.022 in the upper segments), characterising a general mechanism of heavy-metal fixation in the secondary-mineralisation zone.

5. Discussion

5.1. Hypothesis H1: fluorine fixation through CaF_2 precipitation

The combination of independent analytical approaches (ISE for F^- in the effluent; XRF and ICP-MS for the solid phase) confirms that the overwhelming majority of the fluorine introduced with NH_4HF_2 remains within the treated core volume. A direct integral balance for Stage 5 (1250 mg F^- introduced; < 1 mg exported; ≈550 mg fixed in the core by XRF) indicates that about 44 % of the introduced fluorine is fixed in the solid phase. The principal mechanism is calcium-fluoride precipitation via Eqs. (1a)–(1b): sulfuric-acid dissolution of carbonate releases Ca^{2+}, which, as the H^+ activity decreases, is bound by fluoride into fluorite. The Ca depletion in the upper segment (0.186 % against 0.653 %; loss of 0.467 pp) is statistically robust (far exceeding the XRF error of ±0.037 pp at this level), whereas the apparent Ca accumulation in the lower segment (0.724 % against 0.653 %; 0.071 pp) lies within the method error (±0.13 pp) and is not significant; the redistribution conclusion therefore rests on the reliable upper-segment depletion. The F maximum (10–15 cm; 0.139 %) and the nominal Ca maximum (15–20 cm) are offset by one segment: the F maximum falls where the local H^+ activity has decreased enough to permit CaF_2 precipitation ($SI(CaF_2) > 0$) but the SO_4^{2-} activity is still insufficient for pronounced gypsum precipitation; the S maximum (1.383 % against 0.202 %) marks the gypsum zone via Eq. (1c). Thus a two-zone sequence of secondary precipitates is realised — "dissolution → CaF_2 (10–15 cm) → $CaSO_4 \cdot 2H_2O$ (15–20 cm)" — in agreement with the geochemical mechanism computed by Walsh et al. (1982) for oilfield sandstone acidizing.

Additional solid-phase fixation mechanisms may include MgF_2 formation (Mg also accumulates towards the lower segment in the ICP-MS data), F^- adsorption onto kaolinite and hydromica minerals (Tóth et al., 2021), and retention in complex aluminium- and iron-fluoride phases. Direct identification of secondary phases by XRD and SEM-EDS was not performed and constitutes the main limitation in verifying H1. The methodological basis for such verification is given by Zhang et al. (2023) for CaF_2 morphology, Wen et al. (2021) for quantitative EDS mineral identification in tight sandstones, and Menke et al. (2022) for microfluidic dissolution analysis of natural rocks. Direct proof of CaF_2 and amorphous-silica formation in the zones of maximum accumulation and depletion is a priority for further work.

5.2. Hypothesis H2: coupled uranium accumulation in the F-fixation zone

The complete mobilisation of uranium from the upper 5 cm (99.6 % loss at Stage 5) and its preferential retention at 10–15 cm (0.069 mg/g; a 7-fold excess over the adjacent segment)

constitute the key observation of this work. According to Xing et al. (2018) and the summary NEA-TDB data, in acidic, oxidising, F-enriched solutions at T < 200 °C the predominance of uranyl-fluoride complexes $UO_2F_n^{2-n}$ provides the principal mechanism for hydrothermal U transport. In the laboratory ISR system, this implies a two-stage picture: (a) in the upper zone, where high H^+ activity coincides with maximum dissolved F^-, U is mobilised through $UO_2F_n^{2-n}$ complexes; (b) as the solution advances and F^- is precipitated as CaF_2, $[F^-]$ decreases and the equilibrium of Eq. (2) reverses ($UO_2F_n^{2-n} \rightarrow UO_2^{2+}$), which, combined with fresh CaF_2–gypsum phases, creates conditions for co-precipitation and/or sorption of U.

Analogous spatial patterns of changing U speciation with depth are documented for the Hanford 300 Area (Catalano et al., 2006): U was co-precipitated with calcite in the upper segments and occurred as metatorbernite at intermediate depths. Sorption of U(VI) onto freshly formed Fe(III) hydroxides is also described by Bots et al. (2014). Avasarala et al. (2019) showed that bicarbonate-oxidising conditions stabilise U(VI), while the apatite and phosphate barrier technologies of Vermeul et al. (2009) and Shi et al. (2009) offer conceptually similar U-immobilisation routes; the controlling geochemical factors are reviewed by Krupka and Serne (2002). For Kazakhstan's ISR sites specifically, Coral et al. (2022) demonstrated that biostimulation of the autochthonous microflora after acid leaching at the Muyunkum and Tortkuduk deposits neutralises residual acidity and reductively immobilises U, complementing the abiotic mechanism considered here. Quantitatively, the integral balance for Stage 5 shows that ≈11.5 mg of U out of the initial 82.5 mg (about 14 %) remains in the core, with ≈75 % localised at 10–15 cm; the observed effect is therefore a partial local trap rather than a complete geochemical barrier, with the bulk of the U (≈86 %, ≈71 mg) leaving the core. The U balance for the liquid phase is not closed: at the Stage 5 effluent volume (1380 mL) and U concentrations of 12.1–47.9 mg/L (Table 2), the integral export is ≈35–45 mg, whereas ≈71 mg was removed from the core. The difference (≈25–35 mg) is apparently retained in the residual pore liquid not exported during the 9-hour cycle and is partly explained by the approximate averaging of [U]; exact closure requires the interval-resolved calculation $\int[U(t)]\cdot Q(t)\,dt$, a task for further work. From an ISR environmental-safety standpoint, what matters is the spatial pattern: U forms a clear local maximum within the treated volume rather than an extended mobile-U halo. Verification of U speciation by XANES/EXAFS or XPS is necessary to convert H2 into a quantitatively confirmed mechanism.

5.3. Hypothesis H3: destabilisation of the clay fraction at moderate doses

The anomalous minimum of cumulative recovery at Stage 2 (530 mL at 8 g/L; Fig. 2), below the control 740 mL, requires a mechanistic explanation. According to Walsh et al. (1982), above a critical HF concentration the precipitation of sparingly soluble fluorosilicates K_2SiF_6 and Na_2SiF_6 (Eq. 3), as well as $Al(OH)_3$ and AlF_3, occurs. The kaolinite–hydromica fraction has high K^+ and Na^+ in interlayer positions and surface hydroxyls; their rapid release on clay dissolution in a moderate-fluoride medium, combined with a suitable [F^-] level, may cause local supersaturation with respect to K_2SiF_6. A parallel mechanism is colloidal mobilisation of fine clay particles, known for retarded HF systems in oilfield acidizing (Hartman et al., 2006; Underdown et al., 1990): kaolinite and hydromica particles detach, are carried by the flow and plug pore throats, especially in the middle–lower segments.

Direct quantitative proof of either mechanism (fluorosilicate precipitation vs colloidal mobilisation) was not obtained: turbidity, laser diffractometry for particle-size distribution, ζ-potential and SEM-EDS of the outlet-filter deposit were not measured. These experiments will form the next stage and will distinguish the two contributions. The existence of a clear technologically unfavourable regime precisely in the moderate 6–10 g/L range matches the prediction of H3 and agrees qualitatively with Walsh et al. (1982) and Shafiq et al. (2018).

5.4. Hypothesis H4: silicon dynamics and hexafluorosilicic-acid hydrolysis

The non-monotonic response of effluent Si to dose — a minimum of 118 mg/L at Stage 1 (5 g/L) against the control 246 mg/L, followed by a monotonic increase to 822 mg/L at 20 g/L — is an important analytical and geochemical phenomenon. According to Fogler et al. (1975) and Crundwell (2017), silicate dissolution in HF media proceeds with mandatory formation of H_2SiF_6 (Eq. 4). On HF depletion and/or a pH rise, H_2SiF_6 hydrolyses with reverse precipitation of amorphous SiO_2; with excess HF the balance shifts towards fully soluble forms. A fundamental problem is that the standard ICP-MS mode for Si, without special preparation using fluoride-complexing reagents (e.g. boric acid), does not detect the SiF_6^{2-} form, underestimating Si at low doses and producing an apparent “paradoxical” minimum.

With increasing dose, the HF activity and matrix-dissolution intensity rise simultaneously, favouring fully soluble Si forms ($Si(OH)_4$, silica gels) and weakening SiF_6^{2-} masking. A simpler alternative interpretation must, however, be considered: the [Si] minimum at 5 g/L may reflect a

smaller volume of dissolved silicate — at a low dose, HF is insufficient for intense attack on quartz and feldspars, and the measured decrease is real rather than a masking artefact. The two interpretations are not mutually exclusive and cannot be distinguished with the present data; moreover, under standard dilution in 2–5 % HNO_3 a significant fraction of SiF_6^{2-} hydrolyses, weakening the artefact. The [Si] minimum should therefore be regarded as an open question. Total Si should be determined colorimetrically (molybdate method) after alkaline destruction of fluorosilicates, in parallel with direct ICP-MS, to separate the two contributions and close the silicon balance (hypothesis H4).

5.5. Analytical limitations of TISAB-II at high Al and Fe

Ion-selective potentiometry with TISAB-II is a standard for fluoride in natural waters, but at Al > 500 mg/L and Fe > 100 mg/L — typical of ISR lixiviants — it underestimates total soluble fluorine (Kataoka et al., 2009; Patel et al., 2018). TISAB-II contains a citrate complexant that masks Al only partially; at Al > 1000 mg/L in the present effluents, the fraction of F bound into stable AlF_n and FeF_n complexes ($\log\beta_1$ = 6.1 for Al, 5.2 for Fe) amounts to several per cent and is not registered by the ISE. Kataoka et al. (2009) showed that, at Al = 500 mg/L, TISAB-IV (tartrate–Tris buffer) provides 95 % F recovery against ≈70 % for TISAB-II; Patel et al. (2018), on 47 tea samples, found a statistically significant ($p < 0.001$) excess of mean F with TISAB-IV (4.37 mg/L) over TISAB-III (3.54 mg/L), increasing with Al concentration, empirically confirming the buffer's sensitivity to Al–fluoride complexation.

Thus the actual total soluble fluorine in the first samples of Stages 3–5 (15–20 g/L) may exceed the measured 2.4–2.9 mg/L several-fold while remaining in a mobile complex form. This does not negate the conclusion of small F export — the independent XRF confirms ≈44 % solid-phase fixation, with the remainder distributed between fluoride-complex forms and analytically invisible fractions (colloids, SiF_6^{2-}). For complete closure, the ISE should be supplemented by total F determination by ion chromatography after distillation derivatisation. A critical review of methods for distinguishing fluoride species in geological matrices is given by Tóth et al. (2021).

5.6. Mass balance and saturation indices of secondary phases

For Stage 5 (12.5 g/L), the integral fluorine balance, to a first approximation, is as follows. NH_4HF_2 contains two fluorine atoms (molar mass 57.04 g/mol, including 38.00 g/mol F); in acid, HF_2^- dissociates into HF and F^-, and at pH < 3 neutral HF is a substantial fraction, but the total

number of F atoms remains two per molecule. Introduced: 12.5 g/L × 0.4 L × (38.00/57.04) ≈ 3.33 g F. Fixed in the core by XRF: ≈0.11 % × 500 g = 0.55 g F (16.5 %); exported by ISE: < 0.001 g F (< 0.03 %); unallocated residue ≈ 2.78 g F (≈84 %). This deficit is interpreted as: (a) fluoride-complex soluble forms AlF_n and FeF_n — at Al = 2000 mg/L (≈74 mmol/L) and a mean AlF_n coordination number of 1–2, aluminium can bind ≈74–148 mmol/L F (1.4–2.8 g/L), giving a potential capacity of ≈1.9–3.9 g F over 1.38 L, comparable with the entire introduced amount (3.33 g) and invisible to the ISE; (b) the colloidal–gel fraction not exported; and (c) the systematic XRF error (±20 % rel., ±0.11 g). Even under a conservative estimate, free F^- in the productive solution remains below regulatory levels.

F balance item (Stage 5)	F mass (g)	Fraction (%)	Method / basis
Introduced with NH_4HF_2	3.33	100	12.5 g/L × 0.4 L × (38.00/57.04)
Fixed in the core	0.55	16.5	XRF: 0.11 % × 500 g (±20 % rel.)
Exported (free F^-)	< 0.001	< 0.03	ISE with TISAB-II
Bound in AlF_n (calc.)	1.9–3.9	57–117	Al = 2000 mg/L; β(AlF); ISE-invisible
Residue (colloids, SiF_6^{2-}, error)	balance	—	by difference

Table 4. Semi-quantitative fluorine balance for Stage 5. The calculated AlF_n binding capacity (1.9–3.9 g) is comparable with the introduced F (3.33 g) and can account for most of the unallocated residue invisible to the ion-selective electrode. The wide AlF_n range (a factor of ≈2) reflects uncertainty in the mean ligand number and is subject to refinement by PHREEQC calculation.

Quantitative closure requires three independent procedures: (i) thermodynamic speciation of F at the conditions of each effluent fraction in PHREEQC v3 with the llnl.dat database (Parkhurst and Appelo, 2013); (ii) calculation of SI(CaF_2), SI($CaSO_4 \cdot 2H_2O$), SI(SiO_2(am)), SI(AlF_3) and SI($UO_2F_2 \cdot xH_2O$) for each segment from the local pH and pore-water composition; and (iii) total F by ion chromatography for control samples. All three lie beyond the present scope and will form a subsequent publication with full computational databases appended.

5.7. Implications for ISR reactive-transport modelling

The spatial data have direct relevance for calibrating and verifying reactive-transport (RT) models of ISR operations in the Chu–Sarysu basin (Collet et al., 2022; Lagneau et al., 2019; Escario et al., 2023). Collet et al. (2022) applied HYTEC to Tortkuduk and showed that the reactive mineralogical paragenesis (particularly the proportion of Fe oxides) is key to reproducing the U-production chronology; Escario et al. (2023) extended this to forecast the ISR environmental

footprint; Lagneau et al. (2019) demonstrated industrial RT application; and Regnault et al. (2015) addressed process optimisation. None of these explicitly includes fluoride decolmatation: the reagent is treated merely as a permeability "modifier" rather than as an independent, geochemically active component redistributing U, Ca, Al and Fe along the flow.

The present data allow key input parameters to be formulated: (i) the spatial pattern of F fixation, peaking at ≈0.5–0.75 of the effective filtration-path length from the injection point (10–15 cm in the 20 cm column); (ii) a quantitative $Ca^{2+} \rightarrow CaF_2(s)$ transformation coefficient with the local SI; and (iii) a coefficient of local U accumulation in the F-fixation zone. A similar approach was used by Wang et al. (2022) for the Chinese ISR deposit Bayanwula (PHAST code), which likewise showed that uranium predominantly remains within the mined block. The laboratory–reservoir scale comparison remains a fundamental limitation (laboratory: atmospheric pressure, homogeneous charge, isothermal 20–22 °C; reservoir: 5–15 MPa, heterogeneity, 20–35 °C); field verification with core sampling before and after treatment is a necessary next step.

5.8. Study limitations and verification prospects

The limitations and ways to overcome them are: (i) each concentration regime was a single series (n = 1), preventing statistical separation of a reproducible reagent effect from random permeability fluctuation (Hartman et al., 2006; Parkhurst and Appelo, 2013) — the minimal remedy is $n \geq 3$ for the control and optimal regime (12.5 g/L) with standard deviations reported; (ii) direct identification of secondary minerals by XRD and SEM-EDS was not performed, leaving the conclusions on CaF_2, gypsum and amorphous SiO_2 well-founded but indirect (Wen et al., 2021; Zhang et al., 2023; Menke et al., 2022); (iii) total F by ion chromatography and colorimetric Si after alkaline destruction were not performed; (iv) thermodynamic speciation in PHREEQC was not performed; (v) U speciation by XANES/EXAFS was not determined; and (vi) the laboratory scale does not reproduce reservoir conditions. These six directions form the programme of further research and will move the four hypotheses from "well-founded" to "quantitatively verified".

6. Conclusions

(1) Four working hypotheses on the geochemical mechanisms of fluoride behaviour and coupled uranium mobilisation during NH_4HF_2 treatment of uranium ISR wells were formulated and experimentally tested: H1 (CaF_2 fixation), H2 (coupled U retention via $UO_2F_n^{2-n}$ complexes), H3 (clay-fraction destabilisation at moderate doses) and H4 (non-

monotonic Si response through H_2SiF_6 hydrolysis). All four are supported by the data to a first approximation and require quantitative verification by XRD/SEM-EDS, ion chromatography and thermodynamic modelling.

(2) Free fluoride in the effluents during treatment of the weakly cemented sandstone with 5–20 g/L NH_4HF_2 against 40 g/L H_2SO_4 does not exceed 2.9 mg/L in the first sample and decreases to 0.1–1.3 mg/L by the seventh hour; the integral F export by ISE is below 0.1 % of the introduced mass. Given the analytical limitations of TISAB-II at high Al and Fe, the actual fraction of mobile F (including AlF_n, FeF_n, SiF_6^{2-}) may be several times higher, which does not negate the small export.

(3) After the optimal Stage 5 (12.5 g/L), fluorine accumulates in the core to 0.14 % with a maximum at 10–15 cm; calcium is redistributed downward (71.5 % loss in the upper layer), and sulfur increases progressively to 1.38 %, documenting a joint CaF_2–$CaSO_4 \cdot 2H_2O$ fixation mechanism consistent with hypothesis H1.

(4) Uranium is leached by 99.6 % from the upper segment but locally retained in the F-fixation zone (10–15 cm) at 0.069 mg/g, seven times the adjacent segment; the U localisation coincides with the F and Ca maxima, consistent with hypothesis H2 and with the thermodynamic database for $UO_2F_n^{2-n}$ complexes (Xing et al., 2018) and empirical data on U migration in contaminated sediments (Catalano et al., 2006).

(5) Effluent Si depends non-monotonically on dose, with a minimum of 118 mg/L at 5 g/L and a maximum of 822 mg/L at 20 g/L, consistent with hypothesis H4 and the two-stage mechanism $SiO_2 + 6HF \rightleftharpoons H_2SiF_6 + 2H_2O$.

(6) The anomalous minimum of cumulative recovery at 8 g/L (530 mL vs 740 mL in the control) is consistent with hypothesis H3 (secondary colmatation through clay-fraction destabilisation and/or fluorosilicate precipitation); formal confirmation requires direct turbidity, particle-size and SEM-EDS measurements.

(7) An optimal range of 12.5–15 g/L NH_4HF_2 against 40 g/L H_2SO_4 provides maximum filtration recovery (75–86 %) with minimal export of fluorine and associated elements, meeting environmental-safety requirements for fluoride reagents in uranium ISR.

(8) The spatial patterns of F, Ca and U redistribution are proposed as input parameters for extending ISR reactive-transport models (HYTEC, PHREEQC) with explicit treatment of fluoride decolmatation as an independent geochemical component rather than a permeability modifier.

Declarations

Funding and/or Conflicts of interests/Competing interests
This work was supported by the Committee of Science of the Ministry of Education and Science of the Republic of Kazakhstan [grant number AP 22685351].
The authors declare that they have no known competing financial interests or personal relationships that could have appeared to influence the work reported in this paper.

CRediT authorship contribution statement
Zhanibek Seitov: Conceptualization, Methodology, Investigation, Writing – original draft. *Yuriy Permenev:* Supervision, Resources, Project administration. *Zhiger Kenzhetaev:* Investigation, Formal analysis, Validation. *Abay Omarov:* Investigation, Data curation. *Bakytzhan Toktaruly:* Conceptualization, Writing – review and editing, Visualization, Funding acquisition.

Declaration of generative AI and AI-assisted technologies in the manuscript preparation process
During the preparation of this work the authors used a generative AI tool (large language model) in order to translate the manuscript from Russian into English and to improve language and readability. After using this tool, the authors reviewed and edited the content as needed and take full responsibility for the content of the published article.

Acknowledgements

The authors thank the staff of the Centre for Experimental and Applied Methods of the Institute of High Technologies LLP for technical assistance with the column experiments and analytical determinations.

Data availability

Data will be made available on request.

References

Aben, E.K., Yusupov, Kh.A., Rustemov, S.T., 2019. Improving the efficiency of well restoration during uranium recovery by underground leaching. Eurasian Mining 1, 31–34.

Avasarala, S., Torres, C., Ali, A.M.S., Thomson, B.M., Spilde, M.N., Peterson, E.J., Artyushkova, K., Dobrica, E., Lezama-Pacheco, J.S., Cerrato, J.M., 2019. Effect of bicarbonate and

oxidizing conditions on U(IV) and U(VI) reactivity in mineralized deposits of New Mexico. Chem. Geol. 524, 345–355. https://doi.org/10.1016/j.chemgeo.2019.07.007.

Bots, P., Morris, K., Hibberd, R., Law, G.T.W., Mosselmans, J.F.W., Brown, A.P., Doutch, J., Smith, A.J., Shaw, S., 2014. Formation of stable uranium(VI) colloidal nanoparticles in conditions relevant to radioactive waste disposal. Langmuir 30, 14396–14405.

Brookins, D.G., 1988. Eh-pH Diagrams for Geochemistry. Springer-Verlag, Berlin.

Camacho, L.M., Deng, S., Parra, R.R., 2010. Uranium removal from groundwater by natural clinoptilolite zeolite: effects of pH and initial feed concentration. J. Hazard. Mater. 175, 393–398.

Catalano, J.G., McKinley, J.P., Zachara, J.M., Heald, S.M., Smith, S.C., Brown, G.E., 2006. Changes in uranium speciation through a depth sequence of contaminated Hanford sediments. Environ. Sci. Technol. 40, 2517–2524. https://doi.org/10.1021/es0520969.

Collet, A., Regnault, O., Ozhogin, A., Imantayeva, A., Garnier, L., 2022. Three-dimensional reactive transport simulation of uranium in situ recovery: large-scale well field applications in Shu Saryssu Bassin, Tortkuduk deposit (Kazakhstan). Hydrometallurgy 211, 105873. https://doi.org/10.1016/j.hydromet.2022.105873.

Coral, T., Placko, A.L., Beaufort, D., Tertre, E., Bernier-Latmani, R., Descostes, M., De Boissezon, H., Guignot, S., Lagneau, V., 2022. Biostimulation as a sustainable solution for acid neutralization and uranium immobilization post acidic in-situ recovery. Sci. Total Environ. 822, 153597.

Crundwell, F.K., 2017. On the mechanism of the dissolution of quartz and silica in aqueous solutions. ACS Omega 2, 1116–1127.

Escario, S., Seigneur, N., Collet, A., Regnault, O., de Boissezon, H., Lagneau, V., Descostes, M., 2023. A reactive transport model designed to predict the environmental footprint of an in-situ recovery uranium exploitation. J. Contam. Hydrol. 254, 104106. https://doi.org/10.1016/j.jconhyd.2022.104106.

Fogler, H.S., Lund, K., McCune, C.C., 1975. Acidization. III. The kinetics of the dissolution of sodium and potassium feldspar in HF/HCl acid mixtures. Chem. Eng. Sci. 30, 1325–1332. https://doi.org/10.1016/0009-2509(75)85061-5.

Guillaumont, R., Fanghänel, T., Fuger, J., Grenthe, I., Neck, V., Palmer, D.A., Rand, M.H., 2003. Update on the Chemical Thermodynamics of Uranium, Neptunium, Plutonium, Americium and Technetium. Chemical Thermodynamics, vol. 5. OECD Nuclear Energy Agency, Elsevier, Amsterdam.

Hartman, R.L., Lecerf, B., Frenier, W.W., Ziauddin, M., Fogler, H.S., 2006. Acid-sensitive aluminosilicates: dissolution kinetics and fluid selection for matrix-stimulation treatments. SPE Prod. Oper. 21, 194–204. https://doi.org/10.2118/82267-PA.

IAEA, 2016. In Situ Leach Uranium Mining: An Overview of Operations. IAEA-TECDOC-1849. International Atomic Energy Agency, Vienna.

IAEA, 2023. World Distribution of Uranium Deposits (UDEPO). International Atomic Energy Agency, Vienna.

Kataoka, H., Shinohara, A., Kawamura, T., Kanai, T., Sakurai, A., Sato, H., 2009. Determination of fluoride using ion-selective electrodes in the presence of aluminium: comparison of total ionic strength adjustment buffers. Anal. Sci. 25, 1437–1441.

Kenzhetayev, Zh.S., Togizov, K.S., Abdraimova, M.R., Nurbekova, M., 2024. A novel process for decolmatation of wells during in situ leaching of uranium. Min. Miner. Depos. 18, 35–43.

Krupka, K.M., Serne, R.J., 2002. Geochemical Factors Affecting the Behavior of Antimony, Cobalt, Europium, Technetium, and Uranium in Vadose Sediments. PNNL-14126. Pacific Northwest National Laboratory, Richland, WA.

Labrid, J.C., 1975. Thermodynamic and kinetic aspects of argillaceous sandstone acidizing. SPE J. 15, 117–128.

Lagneau, V., Regnault, O., Descostes, M., 2019. Industrial deployment of reactive transport simulation: an application to uranium in situ recovery. Rev. Mineral. Geochem. 85, 499–528.

Langmuir, D., 1978. Uranium solution-mineral equilibria at low temperatures with applications to sedimentary ore deposits. Geochim. Cosmochim. Acta 42, 547–569.

McLeod, H.O., 1984. Matrix acidizing. J. Pet. Technol. 36, 2055–2069.

Menke, H.P., Reynolds, C.A., Andrew, M.G., Pereira Nunes, J.P., Bijeljic, B., Blunt, M.J., 2022. Probing multiscale dissolution dynamics in natural rocks through microfluidics and compositional analysis. Proc. Natl. Acad. Sci. U.S.A. 119, e2202868119. https://doi.org/10.1073/pnas.2202868119.

Migdisov, A.A., Williams-Jones, A.E., Brugger, J., Caporuscio, F.A., 2016. Hydrothermal transport, deposition, and fractionation of the REE: experimental data and thermodynamic calculations. Chem. Geol. 439, 13–42.

Mudd, G.M., 2001a. Critical review of acid in situ leach uranium mining: 1. USA and Australia. Environ. Geol. 41, 390–403. https://doi.org/10.1007/s002540000183.

Mudd, G.M., 2001b. Critical review of acid in situ leach uranium mining: 2. Soviet Block and Asia. Environ. Geol. 41, 404–416.

Parkhurst, D.L., Appelo, C.A.J., 2013. Description of Input and Examples for PHREEQC Version 3 — A Computer Program for Speciation, Batch-Reaction, One-Dimensional Transport, and Inverse Geochemical Calculations. U.S. Geological Survey Techniques and Methods, book 6, chap. A43, 497 pp.

Patel, S., Omid, N., Zohoori, F.V., Maguire, A., Waldron, K.J., Valentine, R.A., 2018. Comparison of total ionic strength adjustment buffers III and IV in the measurement of fluoride concentration of teas. Nutr. Health 24, 89–96. https://doi.org/10.1177/0260106018758781.

Plummer, L.N., Wigley, T.M.L., Parkhurst, D.L., 1978. The kinetics of calcite dissolution in CO_2–water systems at 5 to 60 °C and 0.0 to 1.0 atm CO_2. Am. J. Sci. 278, 179–216.

Regnault, O., Lagneau, V., Fiet, N., 2015. 3D reactive transport simulations of uranium in situ leaching: forecast and process optimization. In: Uranium — Past and Future Challenges. Springer, Cham, pp. 725–730.

Resentera, A.C., Esquivel, M.R., Rodriguez, M.H., 2023. New insights into the thermal behavior and stability of ammonium bifluoride: non-isothermal thermokinetic analysis. J. Therm. Anal. Calorim. 148, 4333–4344.

Schafer, D., Donn, M., Atteia, O., Sun, J., MacRae, C., Raven, M., Pejcic, B., Prommer, H., 2021. Fluoride release from carbonate-rich fluorapatite during managed aquifer recharge: model-based development of mitigation strategies. Water Res. 198, 116880.

Seredkin, M., Zabolotsky, A., Jeffress, G., 2016. In situ recovery, an alternative to conventional methods of mining: exploration, resource estimation, environmental issues, project evaluation and economics. Ore Geol. Rev. 79, 500–514.

Shafiq, M.U., Mahmud, H.K.B., Arif, M., 2018. Mineralogy and pore topology analysis during matrix acidizing of tight sandstone and dolomite formations using chelating agents. J. Pet. Sci. Eng. 167, 869–876.

Shi, Z., Wang, Z., Heald, S.E., Liu, C., Smith, S.C., 2009. Inhibition effect of secondary phosphate mineral precipitation on uranium release. Environ. Sci. Technol. 43, 8344.

Shikika, A., Zabene, F., Muvundja, F., Mwesigye, P., Hai, T., Mulaba-Bafubiandi, A.F., 2021. Extraction of Ta and Nb from a coltan bearing ore by means of ammonium bifluoride fluorination and sulfuric acid leaching. Minerals 11, 1392.

Smith, C.F., Hendrickson, A.R., 1965. Hydrofluoric acid stimulation of sandstone reservoirs. J. Pet. Technol. 17, 215–222.

Taran, A., Kuldeyev, E., Seitkali, N., Kenzhaliev, B., Berkinbayeva, A., 2023. Physico-chemical aspects of uranium extraction for investigation of in-situ leaching scheme realization in Kazakhstan deposits. Complex Use Miner. Resour. https://doi.org/10.31643/2024/6445.12.

Tóth, B., Vass, I., Pap, S., Šolić, M., 2021. Sequential extraction methods for the identification of fluoride binding fractions in geological samples — a critical review. Microchem. J. 168, 106480. https://doi.org/10.1016/j.microc.2021.106480.

Underdown, D.R., Hickey, J.J., Kalra, S.K., 1990. Acidizing chemistry for the deep sandstone reservoirs. SPE Prod. Eng. 5, 251–256.

Vermeul, V.R., McKinley, J.P., Newcomer, D.R., Mackley, R.D., Fruchter, J.S., 2009. An injectable apatite permeable reactive barrier for in situ Sr-90 immobilization. Ground Water Monit. Remediat. 29, 78–88.

Walsh, M.P., Lake, L.W., Schechter, R.S., 1982. A description of chemical precipitation mechanisms and their role in formation damage during stimulation by hydrofluoric acid. J. Pet. Technol. 34, 2097–2112. https://doi.org/10.2118/10625-PA.

Wang, B., Luo, Y., Liu, J.H., Li, X., Zheng, Z.H., Chen, Q.Q., Li, L.Y., Wu, H., Fan, Q.R., 2022. Ion migration in in-situ leaching (ISL) of uranium: field trial and reactive transport modelling. J. Hydrol. 615, 128634. https://doi.org/10.1016/j.jhydrol.2022.128634.

Wen, Q., Liu, X., Zhang, J., Zhao, Y., Liu, Y., 2021. A new quantitative approach for element-mineral determination based on the EDS (Energy Dispersive Spectroscopy) method. Geofluids 2021, 4023704. https://doi.org/10.1155/2021/4023704.

WHO, 2017. Guidelines for Drinking-Water Quality, fourth ed. World Health Organization, Geneva.

World Nuclear Association, 2024. In-Situ Leach (ISL) Mining of Uranium; World Uranium Mining Production. World Nuclear Association, London.

Xing, Y., Mei, Y., Etschmann, B., Liu, W., Brugger, J., 2018. Uranium transport in F-Cl-bearing fluids and hydrothermal upgrading of U-Cu ores in IOCG deposits. Geofluids 2018, 6835346. https://doi.org/10.1155/2018/6835346.

Zhang, W., Hu, Z., Liu, Y., Chen, H., Gao, S., Gaschnig, R.M., 2012. Total rock dissolution using ammonium bifluoride (NH_4HF_2) in screw-top Teflon vials: a new development in open-vessel digestion. Anal. Chem. 84, 10686–10693. https://doi.org/10.1021/ac302327g.

Zhang, X., Li, Y., Wang, J., Liu, H., Chen, F., 2023. Combining seeding crystallization with flotation for recovery of fluorine from wastewater: experimental and molecular simulation studies. Molecules 28, 4490. https://doi.org/10.3390/molecules28114490.